Chapter 3

Sol-Gel Processes of Functional Powders and Films

Chao-Qun Ye

Additional information is available at the end of the chapter

http://dx.doi.org/10.5772/intechopen.69588

Abstract

The key principles of sol-gel process and its characteristics are outlined and its major control parameters are summarized. Different samples of functional powders and films with magnetic, optical, and dielectric properties prepared by the sol-gel method are described. To determine the relationship between microstructure and properties, the effects of preparation conditions on the size and microstructure and electric properties, dielectric properties, optical properties, and magnetic properties are analyzed.

Keywords: sol-gel, magnetic, optical properties, dielectric, CCTO, multiferroics, hexagonal ferrite, $YFeO_3$

1. Introduction

Sol-gel processing is a well-recognized, cost-competitive, bottom-up synthesis technique, which is used in the field of material science and ceramic engineering for the generation of oxide nanopowder and composite NPs from a sol followed by a gel formation [1]. Functionality refers to typical chemicophysical properties owned by materials, which makes them possible to be exploited in technological applications, as in electrical conductors, thermoelectrics, ferroelectrics, magnets, and transparent optical devices. The sol-gel process of functionality opens promising applications in many areas, such as optics, electronics, ionics, mechanics, energy, environment, biology, medicine, for example as membranes and separation devices, fuel and solar cells, catalysts, sensors, and functional smart coatings. Sol-gel-derived coatings provide a wide range of applications, such as corrosion protective, hydrophilic, hydrophobic, antireflective, and antifog coatings; migration barriers against liquid and volatile compounds; antibacterial modification of textiles and water-repellent antistatic textiles; and self-cleaning coatings [2].

The sol-gel method initial study can be traced back to 1846, when Ebelmen find $SiCl_4$ mixed with ethanol in the wet air hydrolysis and formation of gel. The process of making tofu in ancient China may be the first method to use sol-gel technology in a purposeful and effective way; the soybean protein solution was flocculated into a solid bean curd (gel). Until the end of 1930s, W. Geffeken can conduct oxide film preparation through metal alkoxide hydrolysis and gelation. In 1971 in Germany, H. Dislieh reported sol by the hydrolysis of metal alkoxides, after gelation and retreatment in 923–973 K and high pressure resulting in the formation of SiO_2-B_2O_3-Al_2O_3-Na_2O-K_2O multicomponent glass, which aroused great interest and attention in the field of material science. In 1975, B. E. Yoldas and M. Yamane dried the gel to prepare monolithic ceramic materials and porous transparent alumina films. Since 1980s, sol-gel technology has been successfully applied in glass, oxide coatings, and functional ceramic powders, especially composite oxide such as high critical temperature superconducting oxide material synthesis which is difficult to prepare by traditional method.

2. Key principles of sol-gel process and its characteristics

Sol is a system of tiny solid particles suspended in the liquid phase and constantly showing Brownian movement. Because the Gibbs free energy of the interface atoms is higher than that of the internal atoms, the sol is thermodynamically unstable. The particles tend to agglomerate spontaneously, reaching a low surface energy state. If the process is reversible, it is called flocculation; if not reversible, it is called gelation. The gel is a kind of solid feature of the colloidal system composed of fine particles in three-dimensional network structure and a continuous medium consisting of dispersed phase. The transition process to the gel can be briefly described as the formation of the polymer or the particle aggregates formed by the condensation reaction into a small particle cluster and gradually connected to a three-dimensional network structure. Therefore, the gelation process can be regarded as a small particle cluster connected to each other as a continuous solid network.

Sol-gel processes are mainly based on hydrolysis and condensation reactions of metal alkoxides, the molecular precursors that develop an oxide network in a liquid medium [3].

The structures of oxide materials change from nanoparticles to gel according to the reaction rate and the subsequent drying and post-treatment [2, 4–6].

Accurate control of the sol-gel reaction parameters can be designed to produce many forms of certain properties of the materials in the form of glass, fiber, ceramic powder, and thin film (**Figure 1**).

According to the types of precursors, the sol-gel process can be divided into two types: organic and inorganic. The organic route is that the sol-gel is prepared by metal alkoxides which can be considered as a two-step inorganic polymerization. The first step is the hydrolysis of alkoxide ligands to yield hydroxylated metal centers [7]:

$$M(OR)_n + H_2O = M(OR)_{n-1}OH + ROH \quad (1)$$

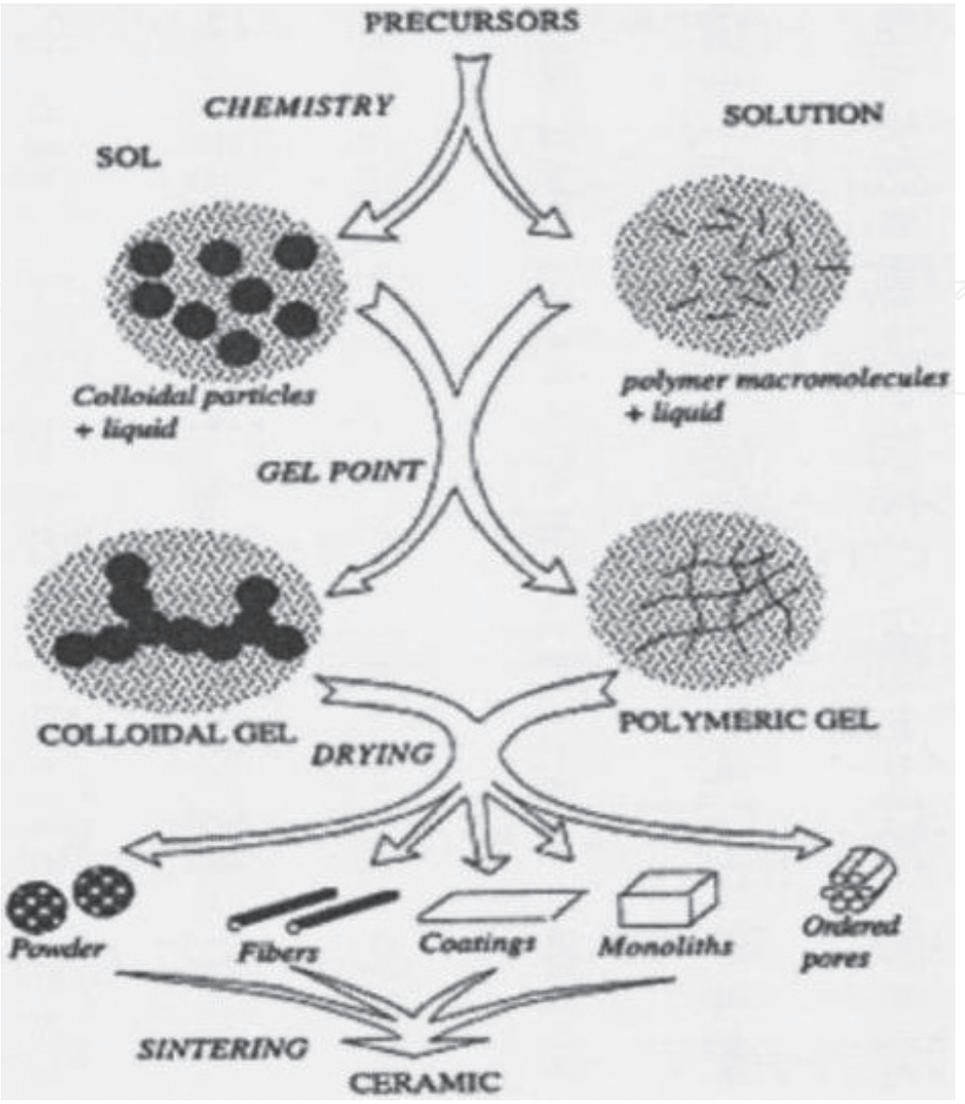

Figure 1. Schematic diagram of the sol-gel process.

The second step is the condensation of the hydroxylated species to form oxypolymers, involving an oxylation reaction which creates oxygen bridges and expels XOH species as follows [7]:

$$M-OH + M-OX = M-O-M + XOH \ (X = H \text{ or } R) \quad (2)$$

3. Major control parameters of sol-gel process

The macroscopic properties of the material are determined by its microstructure, and the microstructure is determined by the conditions of the material.

Generally speaking, the sintering properties of the powder vary in different preparation methods. While using large surface area and high surface activity of monodisperse ultrafine

ceramic powder, due to short diffusion distance and only need lower sintering temperature and activation energy.

Factors that influence the properties of final products, acquired by sol-gel technique, include hydrolysis ratio, acidity of the hydrolyzing agent, gelation condition, drying condition and procedures and types of solvent.

3.1. Chemical compositions of the precursors

The nature of the precursor can significantly affect the sol-gel reaction kinetics and final products.

3.2. Hydrolysis ratio

The hydrolysis ratio, as defined by Eq. (3), is the main external parameter and has been shown to be important in controlling the hydrolysis and condensation of metal alkoxides [5]:

$$h = [H_2O]/[M(OR)_z] \quad (3)$$

where $[H_2O]$ and $[M(OR)_z]$ are the molar numbers for the water and metal alkoxide, respectively; z is the valance charge of metal M.

The lower amount of water added is easy to form the product of low crosslinking, and the viscosity of the sol is increased; the higher amount of water added is easy to form a highly cross-linked product, and the viscosity is decreased. Therefore, the amount of water has an important effect on the structure of the product and the viscosity and gelation time. When $h < 1$, water molecules are not sufficient for complete hydrolysis, and thus gelation or precipitation cannot occur. When $1 < h < z$, chain oxypolymers can form. When $h > z$, cross-linked oxypolymers can be obtained and nanoparticles or gels can be formed. The hydrolysis ratio also has a great influence on the hydrolysis and condensation rate. When h is low (< ~1), the hydrolysis rate is low, so the sol-gel reaction rate including hydrolysis and condensation is also slow. When h is high (< ~7), the hydrolysis rate is high, but the condensation rate is low, the result being a slow sol-gel reaction. When h is intermediate ($1 < h < 7$), the sol-gel reaction is the fastest because of high rates of both hydrolysis and condensation [7].

3.3. Catalysts

Both acids and bases can catalyze sol-gel reactions. The hydrolysis and condensation reactions can be explained by SN2 nucleophilic substitution reaction mechanism. Take alcohol as an example, it is not easy to hydrolyze silicon alkoxide, and its hydrolysis and polymerization are usually catalyzed by acid or alkali. The inorganic acid can make the partially negatively charged alkoxy matrix, so that it is easy to break away from the silicon atom. Alkali provides nucleophilic hydroxyl OH in alkali-catalyzed hydrolysis, and Si—OH loss of protons, thereby accelerating polymerization. In the presence of excess water, because of the acid-catalyzed hydrolysis reaction, Si(OH) can be formed. The rate of polymerization is faster than that of

hydrolysis under the condition of alkali catalysis. Acid or base catalysis is not the only catalyst. Some nucleophiles, such as NaF or 2-methylpyridine, also have the ability to improve the reaction rate.

3.4. pH value

Zinc oxide (ZnO) nanoparticles were prepared and synthesized via sol-gel method, using citric acid as a precursor. The annealing temperature was fixed at 600°C. The impact of pH on the particle size was investigated. Three different pH (3.0, 5.0, and 1.01) for the precursor were chosen, and it was revealed that the Zn NPs size increased with the alkalinity of the precursor [8]. The pH value of the sol-gel solution will change when added with acids and alkalis to catalyze the reactions. Experimental results show that the pH value and hydrolysis ratio have a synergistic effect on the morphologies of the products.

3.5. Reaction temperature

Generally, increasing temperature results in both hydrolysis and condensation rate increase [6, 7].

4. Advantages and shortages of sol-gel processing

The sol-gel process provides samples with high purity, homogeneity, and structure of easy control. The most important advantages of the sol-gel process in the preparation of functional materials are as follows:

(i) In all stages, the temperatures required are low and close to room temperature. Then, thermal decomposition of organic material and any entrapped species is minimized leading to high purity and stoichiometry [2].

(ii) As the organometallic precursors for different metals are miscible, the homogeneous sol solutions are easily achieved [2]. Since the sol-gel is initiated by the reaction of the solution, the materials are very uniform and easy to modify, which is crucial for controlling the physical and chemical properties of the material.

(iii) Precursors such as metal alkoxides and mixed alkyl/alkoxides are easily purified by common techniques (e.g., distillation or sublimation), which lead to high-purity products [2].

(iv) The chemical conditions are mild in sol-gel process. Hydrolysis and condensation are catalyzed by acid or alkali under mild pH conditions [2, 9].

(v) Highly porous and nanocrystalline materials can be synthesized by this method [2].

(vi) Colloid particle size and pore size, porosity, and chemistry of the final product can be optimized by chemical treatment of the precursors, controlled rates of hydrolysis, and by condensation [2].

(vii) Incorporating several components in a single step or in two steps [2].

(viii) Production of samples in different physical forms [2, 10]. Starting from the same raw material, changing the process can get different products, such as fiber, powder, or film and composite materials.

(ix) Treating temperature is low, the inorganic materials can be synthesized under the condition of low temperature at about 600°C, the composition and the structure of the product are uniform, the grain size is small, the activity of the material particles is increased, and the performance of the material is expanded.

(x) Suitable for large-scale industrial production.

The negative factors of sol-gel processing include high precursor cost, overall high cost, and environmental problems associated with the disposal of large quantities of organic by-products. A common theme out of the negative comments was wet chemical processing using alkoxides as precursors [11].

The sol-gel process is more complex in terms of the difficulty in phase control, which is the different chemical and crystal morphology formation at different temperatures. The morphology is relatively simple, generally, spherical particles.

Gelation, drying, and heat treatment take a lot of time to prepare the sample. In the stage of drying and heat treatment, the sample has a great weight loss and residual stress, film prone to cracking and objectively restricting the thickness of thin film and result in film residual porosity.

5. Sol-gel processing of functional powder materials

5.1. Multiferroic properties of powder materials

First, $Y(NO_3)_3 \cdot 5H_2O$ and $Fe(NO_3)_3 \cdot 9H_2O$ were dissolved in deionized water in the molar ratio of n(Y):n(Fe) = 1:1, then citric acid and metal cations were added in the molar ratio of 1.5:1 to dissolve them completely and for the full complexation with metal ions. The acrylamide monomer is added in the ratio of 9:1 to the cation. The mixture at 358 K temperature is heated to polymerize to form a gel at 393 K. The dry gel is crushed into fine powder with a mortar, placed in a muffle furnace with different calcination temperature for 10 h, with the furnace cooling to room temperature to get fine powders of $YFeO_3$. Vibrating sample magnetometer (VSM, Model 7300, Lake Shore) and MPMS magnetic measurement system (SQUID, Quantum, Design) were used at room temperature to measure the temperature curve of the magnetic hysteresis loop. The powder samples and a small amount of ethanol were mixed after grinding and were compressed at a molding pressure of about 300Mpa in the muffle furnace sintering at 923 K and 1173 K for 2 h. Silver paste dried at 353 K was used as the electrode. The sample thickness was about 1.5 mm, and the diameter was about 15 mm. The capacitance and loss were measured by Agilent 4980E LCR analyzer and TH 2617 capacitance measuring instrument, and the temperature and magnetic field were controlled by ET 9000 low-temperature measuring system.

Figure 2 shows the room temperature hysteresis loop and magnetization temperature curve of h-YFO powder. As can be seen from **Figure 2**, h-YFO has a weak magnetism, and the hysteresis loop is narrow and small, which belongs to the soft magnet. The remanent magnetization (Mr) and coercive field (H) are 0.11 memu g^{-1} and 0.19 kOe, respectively. The coercivity and saturation magnetization of possible impurities $Y_3Fe_5O_{12}$ and γ-Fe_2O_3 are about 100 Oe and 26.0 memu g^{-1} and 150 Oe and 70 memu g^{-1} at room temperature, respectively [12, 13].

The magnetization of h-YFO is very small and the coercive field is much larger, so it is possible to exclude the influence of impurities on the magnetic properties of the samples, which is characterizing the magnetic properties of h-YFO.

Figure 3 shows the h-YFO magnetization-temperature relationship curve (M-T) and its first derivative curve (dM/dT-T), measured at the external magnetic field strength of H = 1000 Oe using temperature mode. It can be seen from the figure that the magnetization of h-YFO is gradually reduced from 0.72 memu g^{-1} to about zero in the temperature range of 750 K to 877 K, which indicates that h-YFO has a complex magnetic phase transition in this temperature range.

Figure 4 shows the hysteresis loop and the magnetization temperature curve of o-YFO powder at room temperature. Compared to h-YFO, the hysteresis loop of o-YFO is wide which belongs to hard magnet, and the magnetization and coercive field of o-YFO is 0.72 memu g^{-1} and 24.5 kOe respectively which is much larger than h-YFO. It is also shown that the influence of impurities on the magnetic properties is small. From the extension direction of the loop line, o-YFO has a certain antiferromagnetic property.

It is worth noting that **Figure 4** llustrations for the hysteresis curve of o-YFO on a small magnetic field (<10 kOe) that shows a peculiar shape with a sudden change magnetization in H = 0 kOe, which is considered to be the inherent characteristic of o-YFO. The causes of the abnormal $YFeO_3$ hysteresis loop are produced by the interaction of the same iron ions, the interaction with the external magnetic field, the DM antisymmetric interaction, and the anisotropy effect of the magnetic crystal. The adjacent two iron ions in $YFeO_3$ is of a slight distortion,

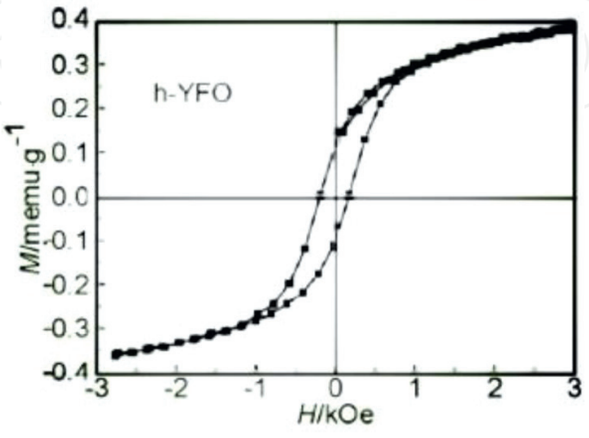

Figure 2. M-H hysteresis curve of h-YFO powder.

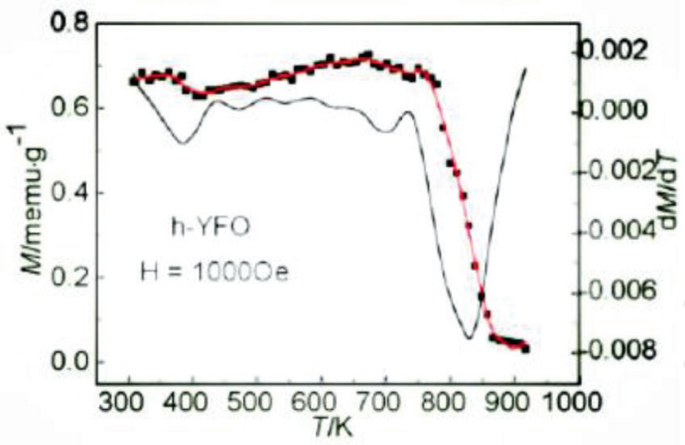

Figure 3. M-T curve of h-YFO powder and its derivative curve.

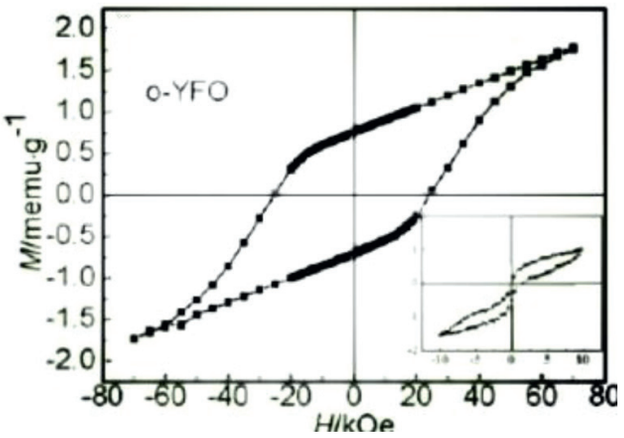

Figure 4. M-H hysteresis curve of o-YFO powder. Inset: M-H hysteresis curve of o-YFO at lower magnetization field.

rather than a strict spin antiparallelly which reveals overall magnetic anisotropy. When the external magnetic field is too small to overcome the anisotropic magnetic field of the magnetic material, the magnetic behavior will be different.

Figure 5 shows the magnetization-temperature curve (M-T) and its first derivative curve (dM/dT-T) for o-YFO, measured in the same way those for h-YFO. The magnetic properties of o-YFO become smaller in the range of 540 K till 645 K, the magnetization is 0, which is similar to the Nair temperature TN = 640 K of the orthorhombic phase YFO, which indicates that the magnetic phase transition process is from antiferromagnetic to paramagnetic.

Figures 6 and **7** show the εr and dielectric loss tan δ of h-YFO variation with temperature in the range of 1 kHz to 300 kHz. It can be seen from the figure that the dielectric constant of h-YFO in the whole frequency range is relatively low, about 10–30, and the dielectric constant and dielectric loss of the sample decrease slightly with the increase in the measurement frequency. In the whole temperature range, there are three obvious dielectric anomalies. The first dielectric anomaly was observed in 125–250 K; the εr-T curve shows the dielectric relaxation and frequency dispersion characteristics. With the

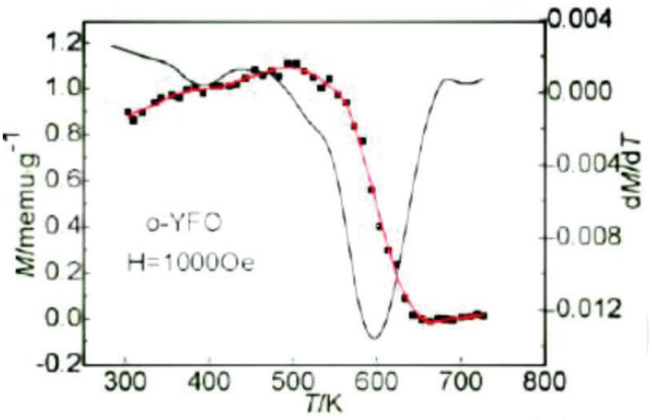

Figure 5. M-T curve of o-YFO powder and its derivative curve.

increase in the electric field frequency, the relaxation peak moves to the high temperature and the peak value decreases gradually. At the same time, the dielectric loss curve also has the corresponding loss peak, the loss peak moves to the high temperature with the increase in the frequency, and the peak value of the loss increases. The second dielectric anomaly appeared between 250 and340 K and h-$YFeO_3$ showed a dielectric anomaly peak at 297 K, and the dielectric peak does not change with the frequency shows that the peak is not caused by the thermal activation, but by a structural phase transition. The third anomalous dielectric is at above 340 K where exists a strong frequency dispersion and the loss increases obviously. It is because the thermal activation mobility of charge carrier increases with the temperature rises, which result in the increase of conductivity. At 300 kHz, the dielectric loss was relatively stable, the main reason was that no electric charge was generated with the change of external electric field. It can be seen from the figure that εr and dielectric loss tan δ of o-$YFeO_3$ have a trend of decline in the highest temperature.

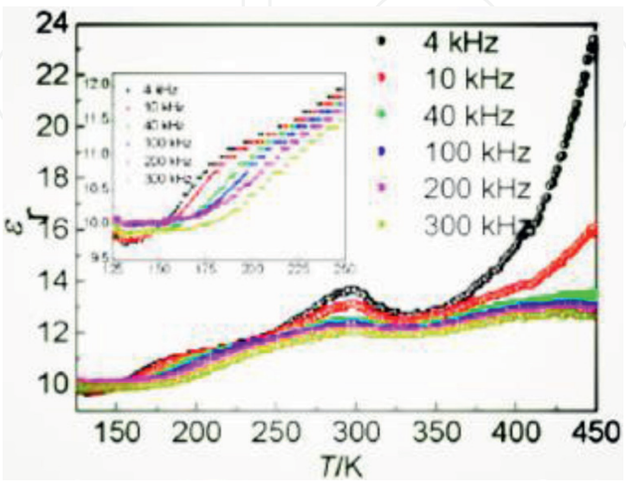

Figure 6. Temperature dependence of dielectric constant εr of h-YFO.

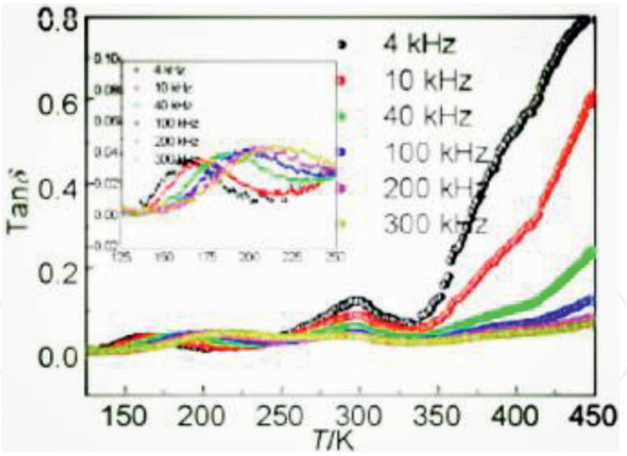

Figure 7. Temperature dependence of dielectric loss tan δ of h-YFO.

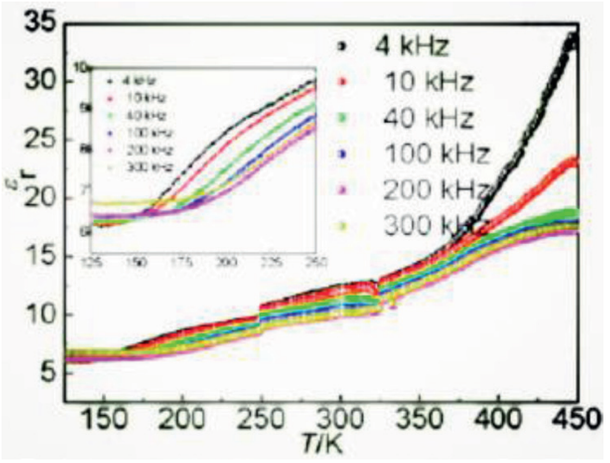

Figure 8. Temperature dependence of dielectric constant εr of o-YFO.

Figures 8 and **9** show the dielectric constant and dielectric loss tan δ r variation with temperature at different frequency from 1 kHz to 300 kHz of o-$YFeO_3$. As can be seen from the figure, o-$YFeO_3$ has two obvious dielectric anomalies in the whole range of temperature. The εr-T curve of o-$YFeO_3$ shows the dielectric relaxation and frequency dispersion phenomenon in the range of 125–340 K. With the increase in electric field frequency, the dielectric constant decreased, the dielectric loss increased, and the dielectric peak shifted to high temperature with the longer dielectric platform afterward. After 340 K, there are second obvious dielectric anomalies, showing a strong frequency dispersion, which is consistent with the change of h-$YFeO_3$. The dielectric relaxation behavior of o-$YFeO_3$ is the result of the decrease of dielectric constant.

5.2. Optical properties of powder materials

For semiconductor nanomaterials, the optical absorption is closely related to the band gap. The short wavelength cutoff in the transmission is due to the fundamental band gap excitation

http://dx.doi.org/10.5772/intechopen.69588

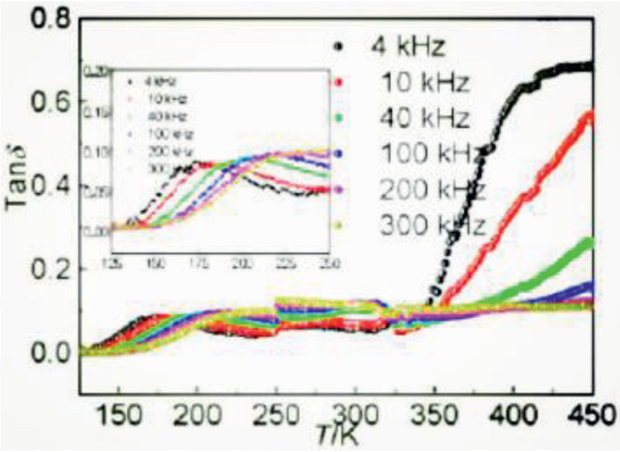

Figure 9. Temperature dependence of dielectric loss tan δ of o-YFO.

from the valence band to the conduction band. Energy band gap of samples can be evaluated from the absorption spectra.

$(La_{(1-x)}Sr_x)(Fe_{(1-x)}Ni_x)O_3$, ($x$ = 0.0, 0.1 and 0.2) NPs were synthesized by sol-gel combustion method. The raw materials were used in analytical grade (AR). Lanthanum nitrate hexahydrate $(La(NO_3)_3 \cdot 6H_2O)$, ferric nitrate nonahydrate $(Fe(NO_3)_3 \cdot 9H_2O)$, strontium nitrate $(Sr(NO_3)_2)$, and nickel nitrate hexahydrate $(Ni(NO_3)_2 \cdot 6H_2O)$ were used as oxidizing agents, whereas citric acid ($C_6H_8O_7$) was used as fuel. All chemicals were completely dissolved in 100 mL diluted water in a beaker under the constant stirrer at 60°C until the homogeneous sol was formed. Ammonia (NH_3) was slowly added to adjust the pH to 7. Afterward, the homogeneous sol was heated at 120°C for 2.5 h. The sol color and viscosity changed and got ignited for further heating automatically. The solid dry gel was calcinated at 600°C in air for 5 h. The UV-Vis absorbance was carried out using Perkin Elmer spectrophotometer [14].

The optical absorption spectra as a function of wavelength of $(La_{(1-x)}Sr_x)(Fe_{(1-x)}Ni_x)O_3$, ($x$ = 0.0, 0.1 and 0.2) NPs is shown in (**Figure 10**). The band gap of semiconductor materials can be estimated by UV-Vis absorption spectroscopy by the Tauc relation given below:

$$(\alpha h\nu)^m = K(h\nu - Eg) \tag{4}$$

where α is the absorption coefficient, K is a constant, m is an integer whose value depends on the nature of transition. The value of m is 2, 1/2, 2/3, and 1/3 for acceptable direct transition, permitted indirect transition, forbidden direct transition, and forbidden indirect transition, respectively [14].

The plots of $(\alpha h\nu)^2$ versus photon energy ($h\nu$) for direct transitions to determine the band gap of the $(La_{(1-x)}Sr_x)(Fe_{(1-x)}Ni_x)O_3$, ($x$ = 0.0, 0.1 and 0.2) NPs are displayed in **Figure 11**, which indicate that the band gap increases with increasing Sr and Ni concentrations. The increase in the band gap could be attributed to the Burstein-Moss effect with an obvious blue shift of the absorption edge [14].

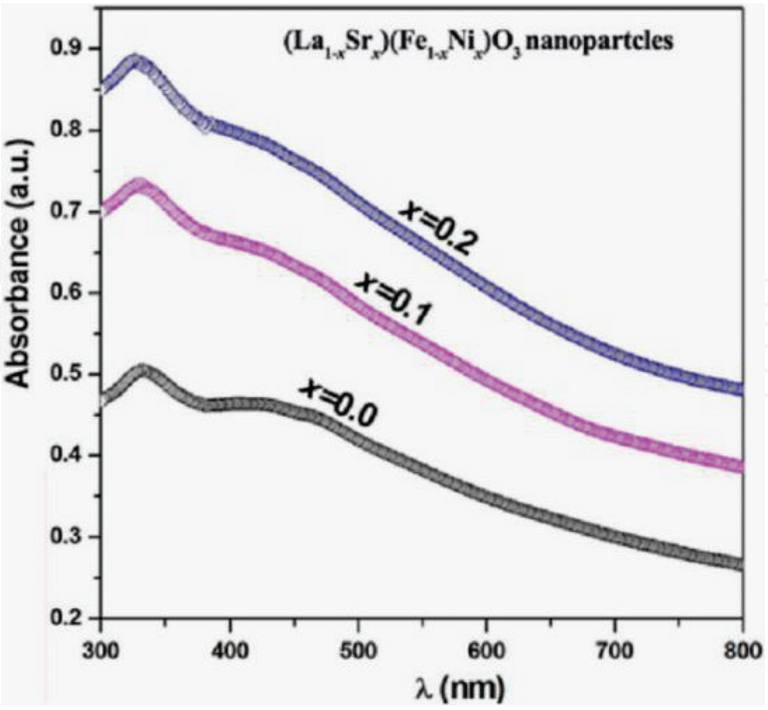

Figure 10. UV-Vis absorption spectrum of the NPs of $(La_{(1-x)}Sr_x)(Fe_{(1-x)}Ni_x)O_3$, ($x$ = 0.0, 0.1 and 0.2).

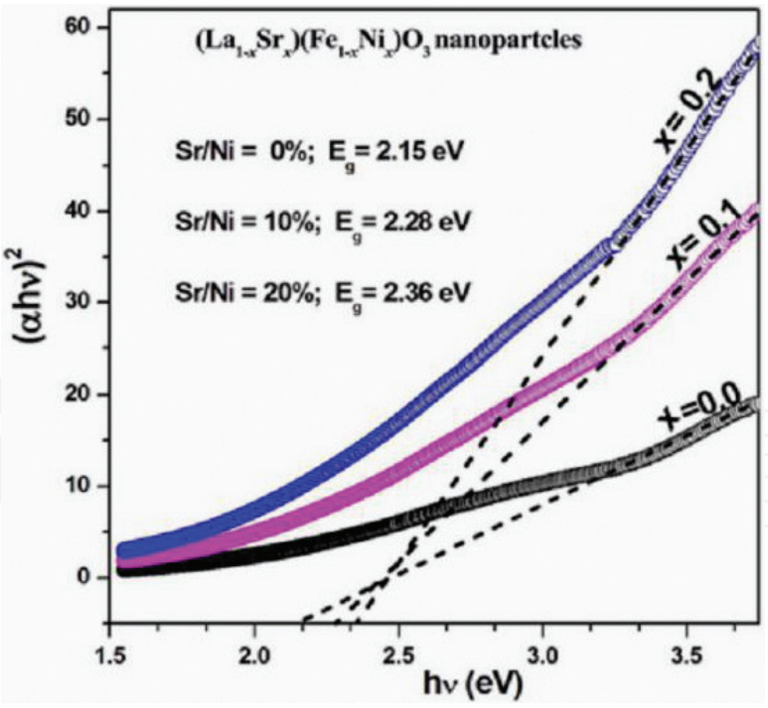

Figure 11. Plot of $(\alpha h\nu)^2$ versus $h\nu$ for NPs of $(La_{(1-x)}Sr_x)(Fe_{(1-x)}Ni_x)O_3$, ($x$ = 0.0, 0.1 and 0.2) NPs.

With the increase in the concentration of doping, the donor states push the Fermi level higher in energy, which shift close to the conduction band above the occupied donor state. In the degenerate semiconductor, only an electron can be excited from the valence band into

conduction band above the Fermi level. Based on the Pauli's exclusion principle this excitation into occupied states is prohibited, resulting in the increase in the optical band gap [14].

6. Sol-gel processes of functional film

Sol-gel-derived coating film is suitable for substrates with large areas. Preferred crystal orientation can be given depending on the conditions of preparation. The techniques can be applied to accomplishing a large variety of functional films with optical, electronic, magnetic, chemical, and mechanical functions.

In sol-gel process, the key film-forming method mainly includes the dip-coating method, the rotating method, the sputtering method, and so on. The dip-coating method is elevating impregnated substrate from uniform solution, after gelling process, to become gel, and the film with nanoparticles can be obtained after a certain temperature, and the film thickness can be controlled by the number of pulling speed or spin coating. The rotation method is a method of liquid film coating on substrate, the film thickness reduces with the increase in the substrate rotation speed. Sputtering is a method of forming film by spraying the solution from one to several stationary sputtering guns onto a preheated substrate which runs at a certain speed.

6.1. Dielectric properties of the perovskite-related oxide CCTO film

Perovskite-related oxide $CaCu_3Ti_4O_{12}$ (CCTO) ceramic has an extremely high dielectric constant (~10,000 for bulk and ~10^5 for single crystals) and moderately lower dielectric loss (~0.1) at low frequencies with centrosymmetric bcc structure (space group $Im\bar{3}$ (no. 204), lattice parameter $a = 0.7391$ nm and $Z = 2$). And it retains its high dielectric constant from 100 to 600 K. Hence, it is capable of potential industrial application for miniaturizing electronic devices [15].

Calcium nitrate ($Ca(NO_3)_2 \cdot 4H_2O$), copper nitrate ($Cu(NO_3)_2 \cdot 4H_2O$), and tetrabutyl titanate ($Ti(OC_4H_9)_4$) were selected as solutes; ethylene glycol monomethyl ether ($CH_3OCH_2CH_2OH$) as solvent; dilute nitric acid as stabilizer; acetic acid as chelating agent; and citric acid as colloidal complexing agent. Zirconium nitrate ($Zr(NO_3)_4$) was used to introduce Zr elements as dopingagents in the sol. Stoichiometric calcium nitrate ($Ca(NO_3)_2 \cdot 4H_2O$) and copper nitrate($Ca(NO_3)_2 \cdot 4H_2O$) were dissolved in methoxyethanol. Subsequently, the solution was heated and stirred to be fully clarified and was cooled to room temperature (select appropriate amount of zirconium nitrate ($Zr(NO_3)_4$) as the introduction of Zr doping agents for the preparation of Zr-doped $CaCu_3Ti4O_{12}$) with a certain dose of dilute nitric acid, and then a stoichiometric amount of tetrabutyl titanate was added. Citric acid ($C_6H_8O_7 \cdot H_2O$) in the ratio of 1:1.5 of sum of the metal ions to the number of moles of citric acid was placed into the solution as complexing agent. By mixing completely, the transparent homogeneous solution of concentration 0.15 mol/L was formed. The solution was aged for 24 h to prepare the powder. Then it was calcined at 450°C for pyrogenic decomposition, and a brown, black powder was obtained. As-prepared powder was made into bulk samples, 10 mm in diameter and 2 mm

in thickness at 20 MPa pressure. Samples were sintered at 1000°C in silicon carbide furnace for 2 h and dense polycrystalline ceramic flakes were formed. The furnace heating rate was 100°C/h and the cooling rate was 150°C/h.

The densities of samples were measured by Archimedes method. The crystalline phases were identified by powder X-ray diffraction analysis installation of a spectrum analyzer with CuK_{α} radiation (λ = 0.154056 nm) (XRD, D/max-IIIC) in a wide range of 2θ ($5° \leq 2\theta \leq 85°$). The samples' microstructure were characterized by SEM (Philips XL30 ESEM-TMP). For the electrical characterization, the ceramics were cut into small pieces of 5 × 5 mm, and gold electrodes with 3 mm radii were sputtered at the center on both sides of each sample. The dielectric properties and impedance analyses were carried out using the precision LCR meter (Agilent 4284A) in the frequency range from 20 Hz to 1 MHz over the temperature range of 150–550 K. The measurement accuracy of the instrument is better than 5%. The dielectric permittivity was evaluated using the standard relation $\varepsilon_r = C \cdot d/(\varepsilon_0 \cdot A)$, where C is capacitance, d is the thickness of the sample, $\varepsilon_0 = 8.854 \times 10^{-12}$ F/m, and A is the effective area of the sample. Dielectric strength measurements were carried out as per the procedure outlined in ASTM D149.

The $CaCu_3Zr_{0.05}Ti_{3.95}O_{12}$ was confirmed by X-ray diffraction. The X-ray diffraction patterns of pure $CaCu_3Ti_4O_{12}$ and $CaCu_3Zr_{0.05}Ti_{3.95}O_{12}$ are shown in **Figure 12**. It shows the room temperature XRD patterns obtained for the $CaCu_3Zr_{0.05}Ti_{3.95}O_{12}$ nanocrystalline powder compared well with the ICDD data (01-075-1149). The samples reveal quite similar diffraction profiles and diffraction peaks corresponding to oxide $CaCu_3Ti_4O_{12}$ phase (JCPDS No. 75-2188) with bcc cubic perovskite-related structure. All the XRD patterns of the main diffraction peaks can be attributed to the CCTO phase. It can determine the crystalline CCTO phase generated. Two curves can be found similar from the figure, which indicate that the content of zirconium has almost no effect on the crystal phase. From the point of view of the ionic radius of Ca^{2+}, Cu^{2+}, and Ti^{4+}, the ionic radius of Ca^{2+}, Cu^{2+}, and Ti^{4+} are l00 pm, 73 pm, and 60.5 pm, respectively, whereas the ionic radius of Zr^{4+} is 79 pm. Through the solution rule of thumb, zirconium is

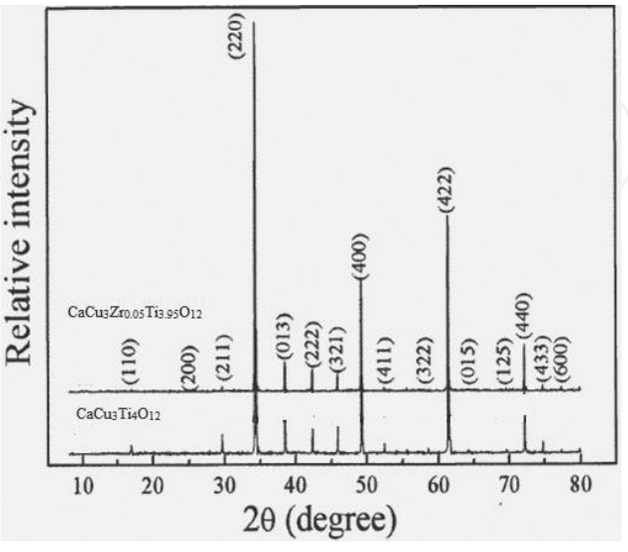

Figure 12. The XRD diffraction patterns for $CaCu_3Ti_4O_{12}$ and $CaCu_3Zr_{0.05}Ti_{3.95}O_{12}$ powder prepared by the sol-gel process.

likely to replace titanium ions at B site belonging to the perovskite ABO_3 structural ceramics in case of the occurrence of solid solution.

The temperature dependence of dielectric properties of $CaCu_3Ti_4O_{12}$ and $CaCu_3Zr_{0.05}Ti_{3.95}O_{12}$ were studied and are illustrated in **Figure 13**. The dielectric temperature spectra of $CaCu_3Ti_4O_{12}$ and $CaCu_3Zr_{0.05}Ti_{3.95}O_{12}$ ceramics were measured at 100 kHz. Dielectric properties' variation with temperature is relatively flat in the range of 100–350 K. As the temperature increases, the thermal stabilities of $CaCu_3Ti_4O_{12}$ and $CaCu_3Zr_{0.05}Ti_{3.95}O_{12}$ deteriorate. The dielectric property stable temperature zone of $CaCu_3Zr_{0.05}Ti_{3.95}O_{12}$ is narrower than that of $CaCu_3Ti_4O_{12}$, whereas the peak width of $CaCu_3Zr_{0.05}Ti_{3.95}O_{12}$ is larger than that of $CaCu_3Ti_4O_{12}$. In the low frequency regime, the dielectric permittivity of $CaCu_3Zr_{0.05}Ti_{3.95}O_{12}$ increased from 50,000 to 500,000 when the temperature was increased from 420 K to 450 K. This sudden increase in dielectric permittivity observed at 100 kHz may be assigned to the space charge/interfacial polarization effects.

Figures 14 and **15** show the frequency dependence of dielectric permittivity and loss at room temperature for pure $CaCu_3Ti_4O_{12}$ and $CaCu_3Zr_{0.05}Ti_{3.95}O_{12}$, respectively. As the frequency increases in the range of 1 KHz to 1000 KHz, the dielectric constant of CCTO-based ceramics decreased. However, the dielectric loss increased significantly with increasing frequency. The dielectric loss of the test samples in the lower frequency at room temperature are relatively closed and nearly keep constant. With increasing frequency, the dielectric constants of pure $CaCu_3Ti_4O_{12}$ and $CaCu_3Zr_{0.05}Ti_{3.95}O_{12}$ decrease rapidly at low-frequency ranges. Both the CCTO-based ceramics possess large dielectric constant in low-frequency ranges, which is attributed to the interfacial polarization at the interfaces between the two components.

As shown in **Figures 3** and **4**, each sample has similar dielectric behavior at room temperature. The dielectric constant displays a steep decrease at a certain frequency, and at the same time the dielectric loss shows a relaxation peak. There is a clear relaxation characteristic and the relaxation is closely related to the measurement frequency, which shows a typical Debye relaxation.

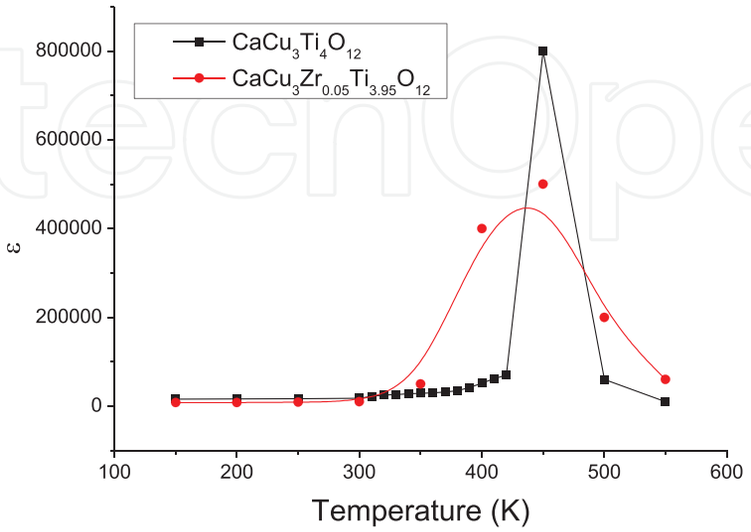

Figure 13. Temperature-dependent dielectric permittivities at 100 kHz for $CaCu_3Ti_4O_{12}$ and $CaCu_3Zr_{0.05}Ti_{3.95}O_{12}$.

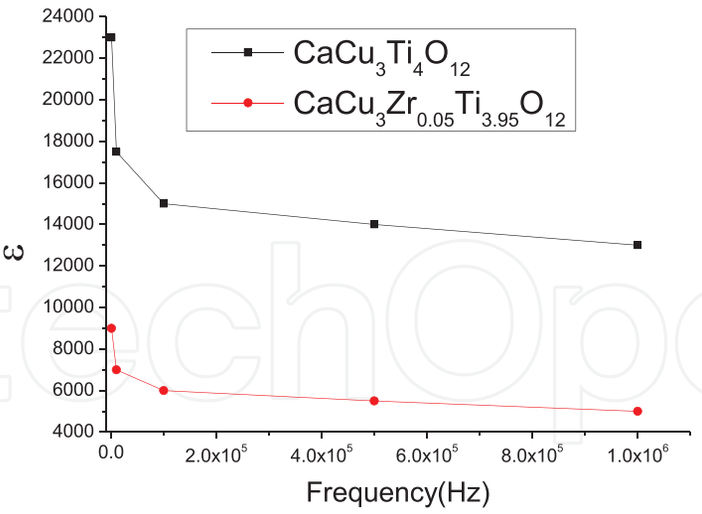

Figure 14. Frequency dependence of room temperature dielectric permittivities for $CaCu_3Ti_4O_{12}$ and $CaCu_3Zr_{0.05}Ti_{3.95}O_{12}$.

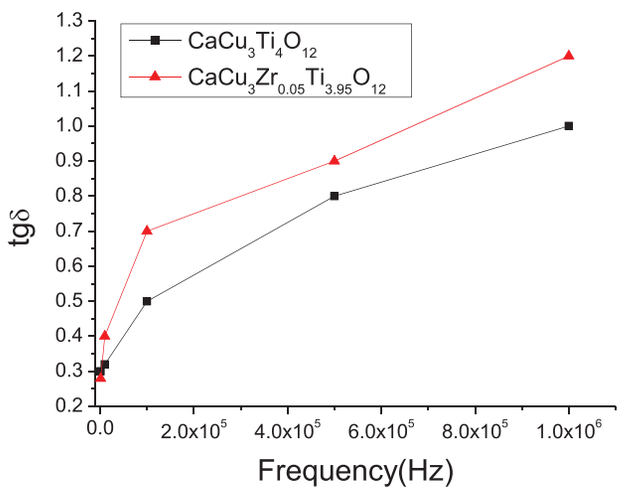

Figure 15. The room temperature dielectric losses for $CaCu_3Ti_4O_{12}$ and $CaCu_3Zr_{0.05}Ti_{3.95}O_{12}$ at various frequencies.

It is obvious that all of these samples exhibit the giant permittivity at low frequency. As the frequency increases, permittivity has a sudden drop in the frequency range below 100 kHz; and then becomes flat. The permittivity increased with decreasing frequency which signaled the possibility of the presence of interfacial polarization. It is probably that the charge carriers may be blocked at an electrode interface when migrated under the influence of an electric field, which causes interfacial polarization. At the same time, the frequency response of dielectric properties of CCTO-based ceramics is closely linked to the polycrystalline microstructure. CCTO ceramics are of very high permittivity, the performance is more obvious especially in the condition of lower frequency, which happens on account of the famous Maxwell-Wagner effect.

It can be seen from the SEM photographs in **Figure 16** that the powder particles are homogeneous and dense, the particle sizes are less than 100 nm estimated from the figure. Crystalline

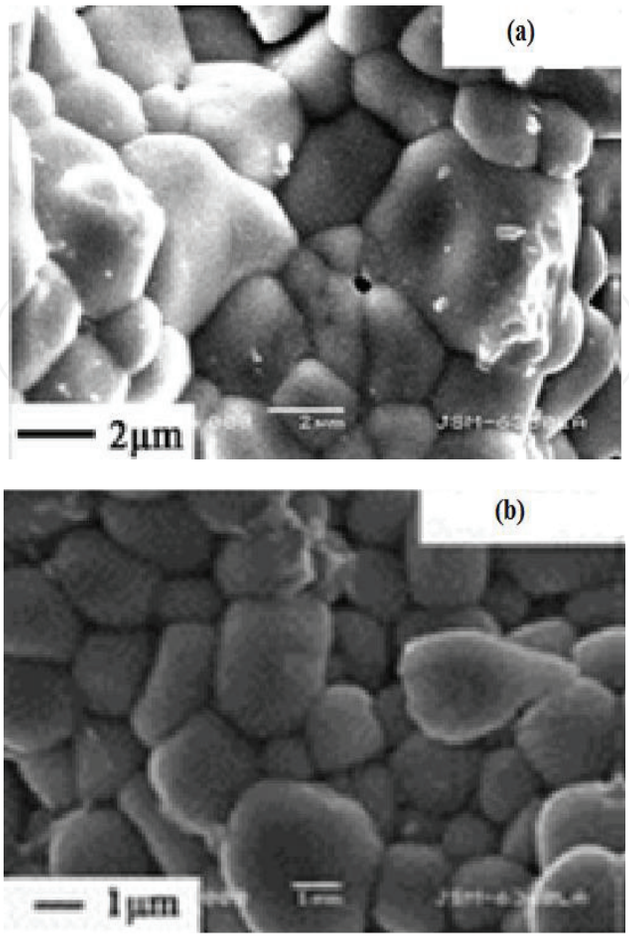

Figure 16. SEM images of CCTO-based ceramics sintered at 1120°C for 2 h. (a) $CaCu_3Ti_4O_{12}$; (b) $CaCu_3Zr_{0.05}Ti_{3.95}O_{12}$.

phase was obtained which can be confirmed from XRD and SEM photographs. The powder prepared by sol-gel process helped in the uniform mixing of all the elements in nanoscale, and corresponding nanocrystals were formed. From the SEM photographs, it is evident that prepared samples of $CaCu_3Ti_4O_{12}$ and $CaCu_3Zr_{0.05}Ti_{3.95}O_{12}$ are composed of many grain, the grain boundary effect can make a major contribution to the high dielectric constant of polycrystalline CCTO-based ceramics.

6.2. Optical properties of magnetic films

Iron-based semiconducting oxide magnetic nanoparticles, for instance spinel ferrites with general formula $M^{2+}(Fe^{3+})_2O_4$ (where M^{2+} = Mn^{2+}, Co^{2+}, Ni^{2+}, Cu^{2+},Zn^{2+}, etc.), have become a prominent family in the magnetic materials due to their high electrical resistivity, high value of magnetic permeability, and use in advanced technologies like microwave devices, magnetic information storage devices, and biomedical applications [16]. Ferrites are one of the most effective photocatalysts for the ejection of toxic dyes from the industrial sewage.

Analytical grade $Fe(NO_3)_3 \cdot 9H_2O$, $(Co(NO_3)_2 \cdot 6H_2O$, $(Mg(NO_3)_2 \cdot 6H_2O$, and citric acid ($C_6H_8O_7$) were used as starting materials for the preparation of $Co_{(1-x)}Mg_xFe_2O_4$ (x = 0.0,

0.3, 0.6, 0.9 and 1.0) ferrites. The molar ratio between metal nitrates and citric acid was adjusted to 1:2. After stoichiometric calculations and weighing, the appropriate quantity of all metal nitrates and citric acid were dissolved in 50 mL deionized water to form a mixed solution. A little quantity of ammonia was included dropwise to maintain the pH value at 7.0. The aqueous solution was heated at 95°C, stirred using a magnetic stirrer, and a viscous solution was obtained. With gel formation, the temperature was raised to 300°C which led to a self-sustaining combustion process followed by the formation of a loose powder. The powder was calcined at 600°C for 6 h with a heating rate of 8.5°C/min resulting in the formation of the final spinel structure samples. Energy band gaps of powder samples were determined using diffused reflection accessory attached with UV-Vis spectrophotometer.

UV-visible spectra were utilized to determine the band gap energies (*Eg*) of all the samples. Diffuse reflection spectra of Mg substituted $CoFe_2O_4$ powder samples were recorded as shown in **Figure 17**. It shows that the *Eg* values were decreased tremendously from 2.4 eV to 1.8 eV with Mg substitution increase that ended in the visible range of e.m. spectra [16].

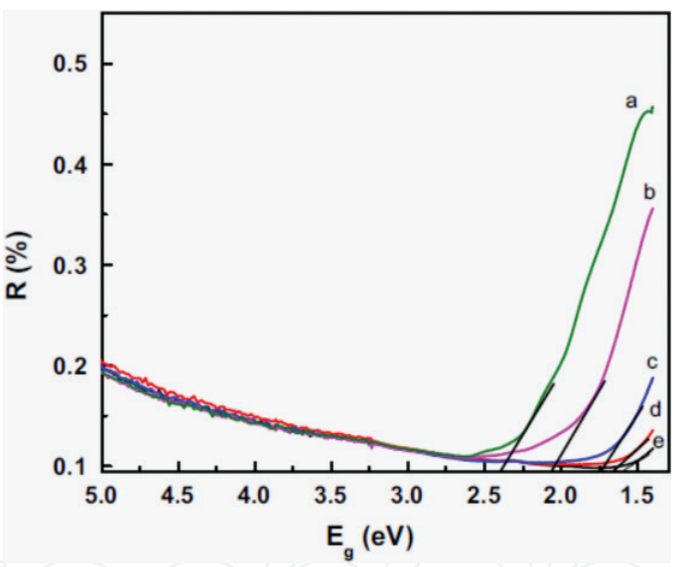

Figure 17. UV-visible diffuse reflectance spectra of $Co_{(1-x)}Mg_xFe_2O_4$ (a) $x = 0.0$, (b) $x = 0.3$, (c) $x = 0.6$, (d) $x = 0.9$, and (e) $x = 1.0$.

7. Conclusion

The preparation methods of the thin films or powders and the heat treatment conditions have a crucial influence on the grain growth of the film. It affects not only the grain size of the film but also the surface morphology of the film, which affects the dielectric properties of the material. Microstructure has effects on the dielectric properties, optical properties, and magnetic properties of samples. Sol-gel method is a reasonable way to prepare function materials. Polycrystalline and nanocrystalline materials can be prepared by this process.

Author details

Chao-Qun Ye

Address all correspondence to: ycq1998@gmail.com

School of Biological and Chemical Engineering, Nanyang Institute of Technology, Nanyang, Henan, People's Republic of China

References

[1] Bhushan, B. Encyclopedia of Nanotechnology, Dordrecht: springer Nature; 2016. DOI: 10.1007/978-94-017-9780-1

[2] Amiri S, Rahimi A. Hybrid nanocomposite coating by sol–gel method: A review. Iranian Polymer Journal. 2016;**25**:6. DOI: 10.1007/s13726-016-0440-x

[3] Rahimi A. Inorganic and organometallic polymers: A review. Iranian Polymer Journal. 2004;**13**:149-164

[4] Rabinovich EM, Klein LC. Sol–Gel Technology for Thin Films, Fibers, Preforms, Electronics and Specialty Shapes. New Jersey, USA: Noyes Publications; 1988. DOI: 10.1016/0025-5408(89)90225-0

[5] Kessler VG, Spijksma GI, Seisenbaeva GA, Hakansson S, Blank DHA, Bouwmeester HJM. New insight in the role of modifying ligands in the sol–gel processing of metal alkoxide precursors: A possibility to approach new classes of materials. Journal of Sol-Gel Science and Technology. 2006;**40**:163-179. DOI: 10.1007/s10971-006-9209-6

[6] Livage J, Henry M, Sanchez C. Sol–gel chemistry of transition metal oxides. Progress in Solid State Chemistry. 1988;**18**:259-341. DOI: 10.1016/0079-6786(88)90005-2

[7] Liu C, Shaw L. Nanoparticulate materials and core/shell structures derived from wet chemistry methods. In: Bharat Bhushan, Editors. Encyclopedia of Nanotechnology. Dordrecht: Springer Netherlands; 2015. p. 1-21. DOI: 10.1007/978-94-007-6178-0_100906-1

[8] Lee K, Guan BH, Zaid HM, Soleimani H, Ching DLC. Impact of pH on zinc oxide particle size by using sol-gel process. In: 4th International Conference on Fundamental and Applied Sciences (ICFAS 2016); 15-17 August 2016; Kuala Lumpur, MALAYSIA. New York: AIP; 2016. p. 1787

[9] Kickelbick G. Hybrid Materials: Synthesis, Characterization and Applications. Weinheim: Wiley; 2007

[10] Xiong J, Das SN, Shin B, Kar JP, Choi JH, Myoung JM. Biomimetic hierarchical ZnO structure with super hydrophobic and antireflective properties. Journal of Colloid and Interface Science. 2010;**350**:344-347. DOI: 10.1016/j.jcis.2010.06.053

[11] Uhlmann DR. The future of sol-gel science and technology. Journal of Sol-Gel Science and Technology. 1997;**8**(1-3):1083-1091. DOI: 10.1007/BF02436988

[12] Nguyet DTT, Duong NP, Satoh T, et al. Temperature-dependent magnetic properties of yttrium iron garnet nanoparticles prepared by citrate sol-gel. Journal of Alloys and Compounds. 2012;**541**(22):18-22. DOI: 10.1016/j.jallcom.2012.06.122

[13] Kishimoto M, Minagawa M, Yanagihara H, et al. Synthesis and magnetic properties of platelet γ-Fe_2O_3 particles for medical applications using hysteresis-loss heating. Journal of Magnetism and Magnetic Materials. 2012;**324**(7):1285-1289. DOI: 10.1016/j.jmmm.2011.11.036

[14] Pankove IJ, Aigrain P. Optical absorption of arsenic-doped degenerate germanium. Physical Review. 1962;**126**(3):956-962. DOI: 10.1103/PhysRev.126.956

[15] Qun YC, Ding L. Dielectric properties of Zr-doped CCTO based ceramics prepared via sol-gel method. Advanced Materials Research. 2012;**528**:121-125. DOI: 10.4028/www.scientific.net/AMR.528.121

[16] Assi H, Atiq S, Rammay SM, Alzayed NS, Saleem M, Riaz S, Naseem S. Substituted Mg-Co-nanoferrite: Recyclable magnetic photocatalyst for the reduction of methylene blue and degradation of toxic dyes. Journal of Materials Science: Materials in Electronics. 2017;**28**(2):2250-2256. DOI: 10.1007/s10854-016-5795-4